ACS APPLIED MATERIALS & INTERFACES

Research Article

www.acsami.org

Exciton-Free, Nonsensitized Degradation of 2-Naphthol by Facet-Dependent BiOCl under Visible Light: Novel Evidence of Surface-State Photocatalysis

Sunxian Weng, ZengXia Pei, Zuyang Zheng, Jun Hu, and Ping Liu*

Research Institute of Photocatalysis, Fujian Provincial Key Laboratory of Photocatalysis−State Key Laboratory Breeding Base, Fuzhou University, Fuzhou 350002, China

Supporting Information

ABSTRACT: Photoreactivity for photodegradation of 2-NAP on BiOCl nanosheets with dominant exposed (010) and (001) facets is studied under visible light via an exciton-free and nonsensitized mechanism. This phenomenon cannot be explained by semiconductor theory or self-sensitized (as those involve dyes) mechanisms. The photocatalytic activities are mainly owing to the formation of the surface state, which is confirmed to be the surface complex Bi−O−$C_{10}H_7$. This surface complex is characterized with ultraviolet−visible diffuse reflectance spectra, Fourier transformed infrared spectroscopy, Raman scattering, X-ray photoelectron spectroscopy, and photoelectrochemical measurement. The optical absorptivity of BiOCl is shifted from the ultraviolet light toward the visible light via a charge-transfer-complex pathway. Charge transfer after the excitation of visible light induces efficient visible photocatalytic activities. The results show that single-crystalline BiOCl nanosheets exposing (010) facets exhibit higher photoactivity due to more surface complex and more terminal bismuth atoms on the surface of BiOCl (010). Our current work is expected to offer new insight into photocatalytic theory for better understandings to photocatalytic reactions and for rational design and synthesis of photocatalyst with high activity.

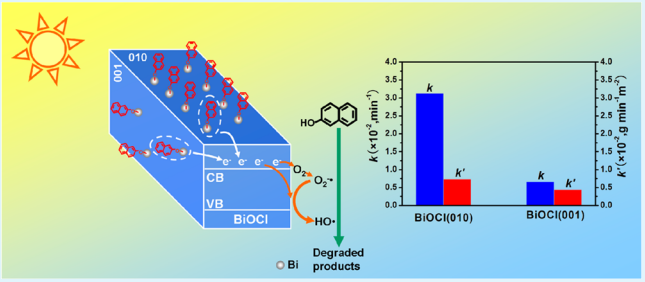

KEYWORDS: *BiOCl, 2-naphthol, visible light, photocatalysis, surface complex*

1. INTRODUCTION

Photocatalysts have long been used to mitigate the deterioration of environment caused by toxic pollutants[1−6] and to alleviate the exhaustion of energy by splitting water for hydrogen production.[7−11] The effectiveness of solar-driven photocatalytic processes underlying hydrogen production and water decontamination is demanded to a large extent via the semiconductors' capabilities of absorbing visible light and their abilities to suppress rapid combination of photogenerated holes and electrons.[1,12,13] BiOCl, which has a layered structure and an indirect-transition band gap to reduce the recombination possibility of the excited holes and electron, is a promising photocatalyst applied to various clean energy and environmental technologies.[14−16] However, the BiOCl photocatalyst can make use of UV irradiation, less than 5% of solar energy, because of its high band-gap energy of 3.46 eV. As a consequence, 95% of sunlight is wasted, which seriously confines the practicability to settle environmental problems. For the sake of increasing the confined optical absorption of BiOCl under solar light, persistent efforts have been made to change the chemical components by adding nonmetal or metal impurities to form acceptor or donor states in the band gap.[12,17] Recent studies have revealed that the optical properties of photocatalysts are able to be manipulated via surface microstructure control engineering, which is different from impurity incorporation.[12,18−20] The catalytic properties of materials are impacted by their superficial microstructures such as morphologies, surface electronic states, defects, and surface complex.[12,21−24] Surface complex, an important active site and light adsorption site for photocatalysis is believed to impact the semiconductor's surface reactivity.[21] Kim and Choi have reported that colorless phenolic compounds were degraded in anatase TiO_2 suspensions under visible irradiation via a surface complex mediated path.[18] So introduced surface complex can broaden the optical absorption of photocatalyst from the ultraviolet light to the visible light. However, the surface complex formation mechanism cannot be explained by the traditional semiconductor theory and has been investigated little.[25] Therefore, it is significant and essential to further look into the theory for better understanding photocatalytic reactions and for rational design and synthesis of photocatalysts with high activity.

The facet effect is also an important factor for heterogeneous photocatalysts, because surface atom arrangement and coordi-

Received: August 3, 2013
Accepted: November 15, 2013
Published: November 15, 2013

nation intrinsically determine the adsorption of reactant molecules.[26−30] Theoretical and experimental research have demonstrated that in contrast to BiOCl (001) surface, the surface of BiOCl (010) consists of more terminal bismuth atoms rather than terminal oxygen atoms, and these terminal bismuth structures can serve as active sites for photocatalytic reactions.[14] Thus, BiOCl with a high proportion of (010) facets is highly desirable.

In this paper, we report a novel example to use the BiOCl photocatalyst for degradation of 2-naphthol (2-NAP) under the illumination of visible light. Meanwhile, we present the results of our investigation on the facet-dependent photoreactivity of the BiOCl under visible light illumination. Further research revealed that the visible light activity of the 2-NAP/BiOCl system is correlated with the change of surface state (surface complex formation), which is supported by a series of joint techniques. This phenomenon provides a novel evidence of surface-state photocatalysis, which may offer new insight into photocatalytic theory.

2. EXPERIMENTAL SECTION

Materials. Potassium Chloride (KCl), Bismuth nitrate pentahydrate ($Bi(NO_3)_3{\cdot}5H_2O$), 2-naphthol (2-NAP), 2,3-dihydroxynaphthalene, 1-naphthol, and acetonitrile were purchased by Sinopharm Chemical Reagent Co. Deionized water was used throughout this study. 5,5-Dimethyl-1-pyrroline *N*-oxide (DMPO) was used as radicals spin trap and obtained from Alfa Aesar. Other chemicals were of analytical reagent grade without further purification.

Preparation of Photocatalysts. BiOCl nanosheets with dominant exposed (010) facets were fabricated via an early reported approach.[14] In this synthesis, 1 mmol $Bi(NO_3)_3{\cdot}5H_2O$ and 1 mmol KCl were added in 19 mL of deionized water at room temperature with continuous stirring, and then 1 M NaOH was dropped into this solution in order to monitor the pH value of solution to about 6.0. The mixture solution was stirred for 1h and then poured to a 28 mL Teflon lined stainless autoclave. The autoclave was allowed to be heated up to 160 °C and kept at 160 °C for 24 h under spontaneous pressure. Then the autoclave was cooled to room temperature in the air. The resulting products were gathered and rinsed using deionized water and ethanol for several times. The products were finally transferred to a 60 °C oven in the air for 12 h. The product obtained was denoted as BiOCl (010). In addition, the product was obtained without the addition of NaOH solution under the same condition and was denoted as BiOCl (001).

Characterization. The crystal phase structures of products were recorded on Bruker D8 advance X-ray diffractometer with Cu Kα radiation operated at 0.04 A and 40 000 V. The XRD data was collected on the 2 theta region from 10° to 70° using a 0.02 scan step width per second. The morphologies of the samples were performed by a field-emission scanning electron microscope (SEM) (FEI Nova NanoSEM-230). Transmission electron microscopy (TEM) and high-resolution transmission electron microscopy (HR-TEM) images were performed by a FEI TecnaiG2F20 S-TWIN with a 200 000 V accelerating voltage. Electron-spin resonance (ESR) signal measurement was carried out on a Bruker A300 model spectrometer. The radicals were trapped through adding DMPO and detected under the visible light ($\lambda \geq 420$ nm) with a 300 W xenon lamp (PLS-SXE300, Beijing Perfect-Light Co.). The microwave frequency, center field, and power were 9.86 GHz, 3512.48 G, and 6.35 mW, respectively. The light absorption properties of the products were carried out on an ultraviolet−visible diffuse reflectance spectroscopy (UV−vis DRS) with an ultraviolet−visible spectrophotometer (Lambda 950, PerkinElmer Co.). $BaSO_4$ was selected as the background. XPS characterizations are determined by an ESCALAB 250 photoelectron spectroscope system. Zeta potentials of the products were performed on Zeta-sizer-3000HSA instrument at ambient temperatures. The concentration of the sample solution was about 1 g L^{-1}. N_2 sorption analysis was carried out at 77 K using ASAP-2020 and was operated with the BET approach. The Fourier transform infrared spectroscopy (FTIR) data were collected with a resolution of 4 cm^{-1} using a nicolet Nexus-670 FTIR spectrophotometer. The Raman scattering measurement was measured on a Renishaw instrument with a 532 nm laser at ambient temperatures. The collection of the scattered light and laser beam were obtained by a 50× microscope objective lens. The time of obtained spectra was 5 s, and the spot radius of samples was 0.5 μm under the focused laser-beam irradiation. Photocurrent was carried out on the self-made three electrode quartz cell by the BAS Epsilon workstation. The indium−tin oxide (ITO) conductor glass, Ag/AgCl electrode, and platinum foil plate were used as the working electrode, reference electrode, and counter electrode, respectively. Twenty milligrams of sample powder was dispersed into 200 uL of *N*,*N*-dimethylflormamide (DMF) under ultrasonication for 1 h to obtain slurries. The as-prepared slurries were spread onto the surface of ITO glasses to obtain sample films with the region of 0.5 × 0.5 cm, whose edge parts were preprotected by Scotch tape. These as-prepared ITO glasses electrodes were fired at 80 °C for 30 min and then dried at 120 °C for 60 minutes under ambient conditions to improve adhesion. The electrodes without coated slurries were isolated using epoxy resin. The 200 mM Na_2SO_4 (pH = 6.8) was used as the electrolyte solution. A xenon lamp (300 W) with a 420 nm cutoff filter was employed as a visible light photosource. For the characterization of 2-NAP adsorbed over BiOCl, the sample was prepared as follows: 100 mg of the sample was dispersed into 100 mL with a 5.0×10^{-5} mol L^{-1} 2-NAP solution (solvent: H_2O/acetonitrile = 9999/1 v/v) for 1 h to establish an adsorption−desorption equilibrium, filtered, and then dried at 80 °C for 4h.

Photocatalytic Activity Measurements. The photocatalytic activities of BiOCl exposing different facets were evaluated using photodegration of 2-NAP under the irradiation of visible light. The PLS-SXE300 xenon lamp (300 W, Beijing Perfect-Light Co.) with an ultraviolet cutoff filter was employed as the light source to offer a wavelength $\lambda \geq 420$ nm visible light. Typically, 0.08 g of photocatalysts was added to 80 cm^3 2×10^{-5} mol/L of 2-NAP solution (solvent: H_2O/acetonitrile = 9999/1 v/v) in a quartz container. To establish an adsorption−desorption equilibrium, the suspensions would be stirred without irradiation for 60 min prior to illumination. During the procedure of degradation, 3 cm^3 suspensions were gathered per 20 min and the concentration of 2-NAP was monitored on an ultraviolet−visible Varian Cary-50 spectrophotometer after centrifugation. A TOC-VCPH analyzer (Shimadzu Co.) was used to analyze the total organic carbon (TOC) of the degradation.

3. RESULTS AND DISCUSSION

The BiOCl nanosheets with different dominant exposed facets are successfully prepared via a hydrothermal method.[14] The crystal structure and morphology of the BiOCl nanosheets are analyzed with the XRD, SEM, and TEM, respectively. In addition, we have previously reported the morphology and crystal structure of BiOCl (001).[15] The SEM and TEM photographs (Figure 1a,b) of BiOCl (010) nanocrystal show that the morphology of BiOCl consists of nanosheets, and the thickness and width of nanosheets are estimated to be 20−80 and 200−1000 nm. The corresponding SAED pattern (Figure 1c) along the [010] zone axis shows (102) and (002) planes with a 43.4° interfacial angle, which is consistent with the calculated value by theory. Figure 1d is the HR-TEM image of BiOCl (010), which displays that the lattice spacing is ca. 0.37 and 0.27 nm, which is identical to the corresponding (002) and (102) of BiOCl, respectively.[14] Therefore, the as-prepared BiOCl nanosheets are covered with dominant (010) facets.

The XRD was employed to determine the crystallographic phase of the products. The XRD patterns of BiOCl (010) and BiOCl (001) are displayed in Figure 2. All the sharp diffraction peaks are well indexed to the phase of BiOCl, corresponding to

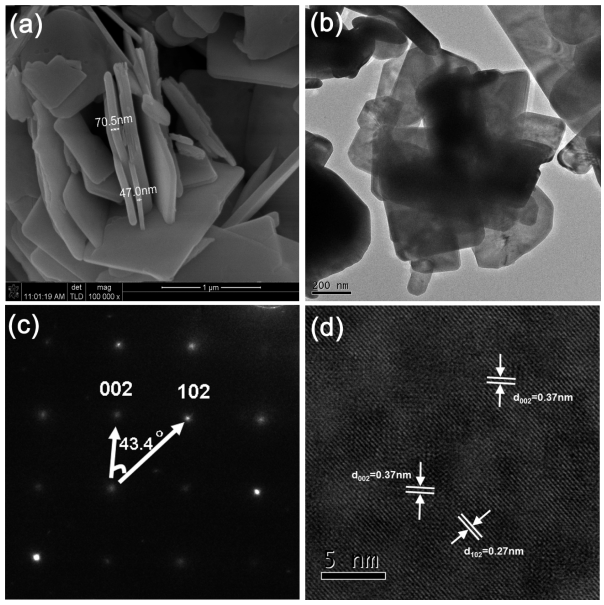

Figure 1. Electron microscope image of the BiOCl (010): (a) SEM, (b) TEM, (c) SAED, and (d) HR-TEM.

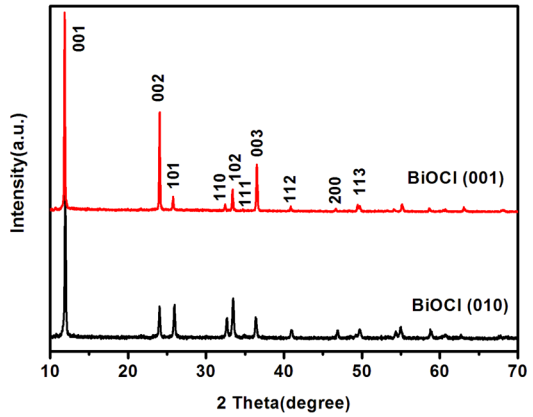

Figure 2. XRD patterns of BiOCl (001) and BiOCl (010).

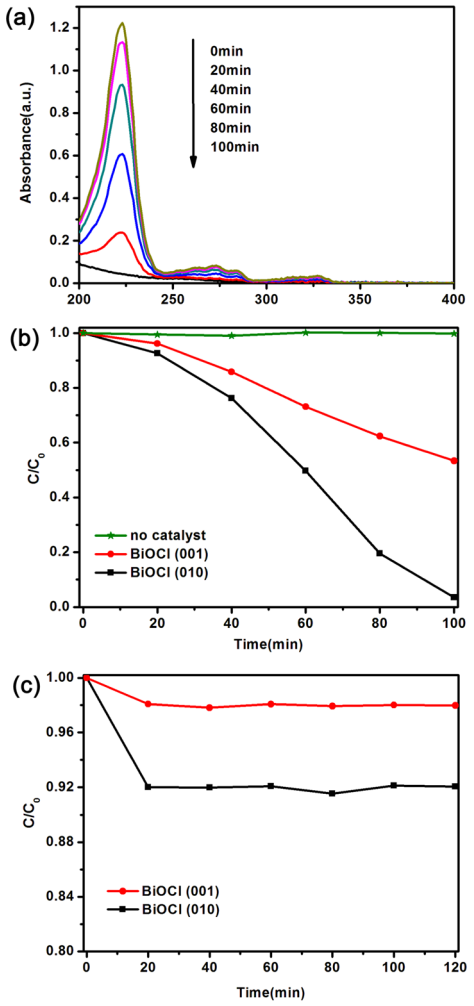

Figure 3. (a) UV−visible adsorption shifts for 2-NAP solution (2×10^{-5} mol L^{-1}) as a function of visible irradiation time with BiOCl (010). (b) Time profiles of photocatalytic degradation of 2-NAP over BiOCl (001) and BiOCl (010) under visible light irradiation. (c) Time profiles of adsorption of 2-NAP over the BiOCl (001) and BiOCl (010) in the dark.

the standard JCPDS: 06-0249 (space group: *P*4/*nmm* (129), $a = b = 0.3891$ nm and $c = 0.7369$ nm, $z = 2$). The result indicates that the BiOCl phase is the main phase in the products due to no peak of other phases detected. The intensity proportions of the (200) peak and (002) peak are 0.332 and 0.046 for BiOCl (010) and BiOCl (001), respectively. These different intensity proportions reflect the different surface structures between BiOCl (010) and BiOCl (001), which is identical to the HR-TEM and SAED results. Surface property is a vital factor for photocatalytic performances of semiconductors, which is easily affected by its distinct exposed crystal facets.[14,26−30]

2-NAP, which widely originates from numerous industrial activities, is poisonous and severely harmful to a human kidney and liver.[31] Therefore, 2-NAP should be settled prior to being recycled or discharged into the environment. Figure 3a shows the temporal absorption spectra of 2-NAP solution in the presence of the BiOCl (010) (content: 1 g L^{-1}) under visible light illumination at room temperature. From Figure 3a, it can be found that colorless 2-NAP in solution is gradually photodegraded. In the absence of a catalyst, the photodegradation of 2-NAP is negligible (see Figure 3b) under visible light illumination. After 100 min, as displayed in Figure 3b, the degradation percentages of 2-NAP are 99.0% and 50.2% with the existence of BiOCl (010) and BiOCl (001), respectively. Furthermore, the extent of mineralization is evaluated by measuring the total organic carbon (TOC). After visible irradiation for 100 min, the TOC value of the final solution for BiOCl (010) is 3.93 mg L^{-1}, whereas it is 6.78 mg L^{-1} for BiOCl (001). The initial total organic carbon of 2-NAP is 8.65 mg L^{-1}. The corresponding mineralization efficiency is evaluated to be ca. 54.5% for BiOCl (010) and 21.6% for BiOCl (001). It is clearly demonstrated that the BiOCl (010) shows a better performance, with an apparent quantum yield (AQY) of 1.2% measured at 420 nm. The results suggest that the visible light reactivity of 2-NAP might be associated with the change of surface state (such as surface complex formation) because BiOCl and 2-NAP cannot absorb the visible light.

Specific surface area is always a vital influencing factor in photocatalysis. The results show that the BET specific surface areas for the as-prepared BiOCl (010) and BiOCl (001) are ca. 4.3 m^2 g^{-1} and ca. 1.5 m^2 g^{-1} respectively. To describe the photocatalytic performance more accurately, the initial reaction rate of photocatalytic degradation is investigated. For the low

concentration of the original solution, the photocatalytic reactions are supposed to accord with a first-order reaction kinetics model and the result is illustrated in Figure S1 (Supporting Information). The degradation constant of BiOCl (010) ($k' = 7.2 \times 10^{-3}$ g min^{-1} m^{-2}) is much higher than that of BiOCl (001) ($k' = 4.3 \times 10^{-3}$ g min^{-1} m^{-2}) after normalization with surface areas. It suggests that the photocatalytic activities of BiOCl are associated with surface structures rather than surface area.[14]

To gain further information for the facet-dependent photoreactivity of the BiOCl, we scrupulously investigated the procedure of 2-NAP adsorption on BiOCl (010) and BiOCl (001). The result (Figure 3c) reveals that the adsorption ability of 2-NAP over BiOCl (001) is lower than that for BiOCl (010), which may be related to the active sites over the BiOCl surface. The calculations of 2-NAP adsorption capacity are about 0.24 and 0.06 mg/g for BiOCl (010) and BiOCl (001), respectively. Some studies[14] indicate that the surface structures of BiOCl (001) contain a considerable amount of terminal oxygen atoms, which will result in more negative charges than for BiOCl (010). This structural characteristic is confirmed by zeta potential (Figure S2, Supporting Information). The repulsive interaction between the anionic 2-NAP and the negatively charged surface (001) is liable for the low adsorption capacity of 2-NAP over BiOCl (001). In contrast, the BiOCl (010) surface atomic structures present more terminal bismuth atoms, offering more active sites for formation of the surface state on BiOCl (010) surface, which is identical to the DRS, FTIR, Raman, and XPS analyses below.

The optical property of the surface complex formed over BiOCl is distinguished by DRS. It can be observed that the existence of 2-NAP leads to the extra consecutive visible light absorption from 400 to 800 nm (Figure 4). 2-NAP/BiOCl

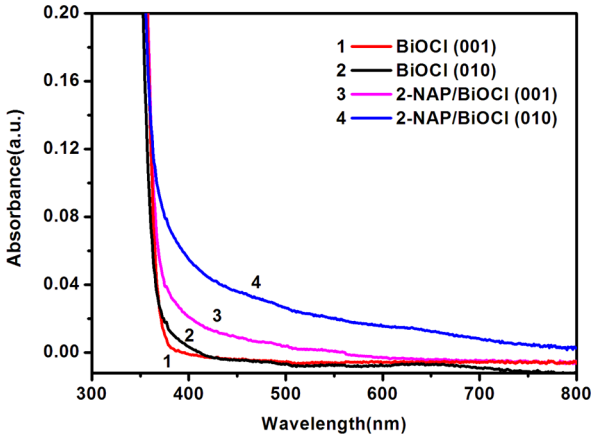

Figure 4. UV–visible DRS of BiOCl and 2-NAP/BiOCl.

(010) exhibits a stronger visible light absorption intensity than 2-NAP/BiOCl (001), suggesting that it will possess a higher photocatalytic activity for target reactions. This hypothesis is confirmed by the degradation and photocurrent of 2-NAP over the BiOCl (010) and BiOCl (001) under the same conditions. This absorption indicates the formation of surface complex resulting from BiOCl (010) and 2-NAP compounds, like 4-CP/TiO_2.[18] The structure of the surface complex is most likely to be that 2-NAP is linked to BiOCl surface via the dehydration reaction as shown as following equations.

$$-\mathrm{Bi}-\mathrm{OH} + \mathrm{HO}-\mathrm{C_{10}H_7} = -\mathrm{Bi}-\mathrm{O}-\mathrm{C_{10}H_7} + \mathrm{H_2O} \quad (1)$$

Figure 5 displays the FTIR spectra for the products, BiOCl (010), the as-prepared 2-NAP/BiOCl (010) composite, and 2-

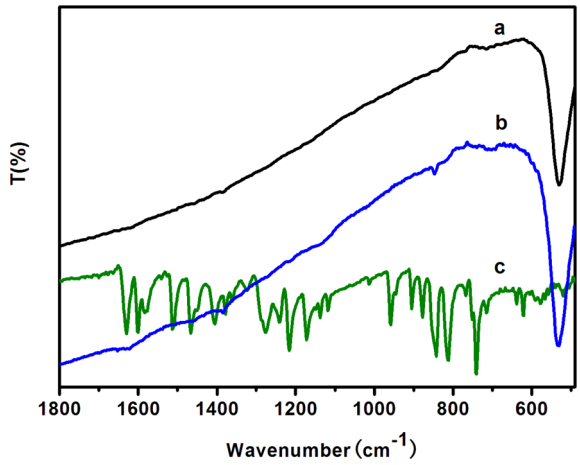

Figure 5. FTIR spectra for (a) BiOCl (010), (b) 2-NAP/BiOCl (010), and (c) 2-NAP.

NAP obtained by the reference method. The strong absorption bands around 520 cm^{-1} should be considered as the vibrations of chemical bond in BiOCl;[32] both can be seen in BiOCl (010) and 2-NAP/BiOCl (010). The absorption band appearing around 847 cm^{-1} (curve b) could be considered the bending vibration of C–H bonds,[33] whereas there is none for the BiOCl. Curve b also shows the weak stretching vibrations of the aromatic ring (1400–1600 cm^{-1}), the weak stretching vibrations of the phenolic group (1160–1300 cm^{-1}), and the weak bending vibrations of C–H bonds (1100 cm^{-1}) due to weak adsorption capacities of 2-NAP.[33] The disappearance of FTIR peaks (such as γ(O–H), 741 cm^{-1}, δ(O–H), 1633 cm^{-1}) to the naphtholate groups is observed in 2-NAP/BiOCl (010). The FTIR data also suggest the surface complex formed over BiOCl surface via a naphtholate linkage, as displayed in eq 1.[20] The conclusion is further demonstrated via XPS measurements and Raman spectroscopy.

To determine the surface structural changes before and after adsorption, a Raman spectrum investigation is utilized for the as-prepared samples. For the Raman spectrum of all the samples, there is one weak band and three distinguished bands. Similar to the reported value,[34−37] the three distinguished bands located at 146, 50, and 201 cm^{-1} belong to the A_{1g}, external A_{1g}, and E_g internal Bi–Cl stretching mode, respectively. Although, the E_g and B_{1g} band at about 398 cm^{-1} is very weak due to the motion of oxygen atoms. For the 2-NAP/BiOCl (001) and 2-NAP/BiOCl (010), new bands located at 500–1700 cm^{-1} are observed in Figure 6a,b. These Raman bands cannot belong to any BiOCl. And the new bands are inconsistent with 2-NAP. These results indicate that structural changes occur presumably owing to the formation of the surface complex.

The XPS characterization provides further insight into the assessment of the surface composition and purity of the product. The peak of C 1s (284.6 eV) is derived from the adventitious carbon on the BiOCl surface. The C 1s spectra of the 2-NAP/BiOCl (010) (Figure 7a) and 2-NAP/BiOCl (001) (Figure 7c) can be deconvoluted into three peaks corresponding to C=C/C–C, C–H, and C–O, with binding energies of 284.6, 286.3, and 288.4 eV for the 2-NAP/BiOCl (001), and 284.6, 286.1, and 288.4 eV for the 2-NAP/BiOCl (010).[38,39]

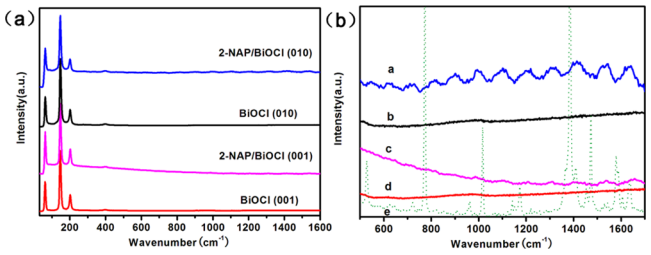

Figure 6. (a) Raman spectrum of samples and (b) detail of partial magnified panel a: a, 2-NAP/BiOCl (010); b, BiOCl (010); c, 2-NAP/BiOCl (001); d, BiOCl (001); e, 2-NAP.

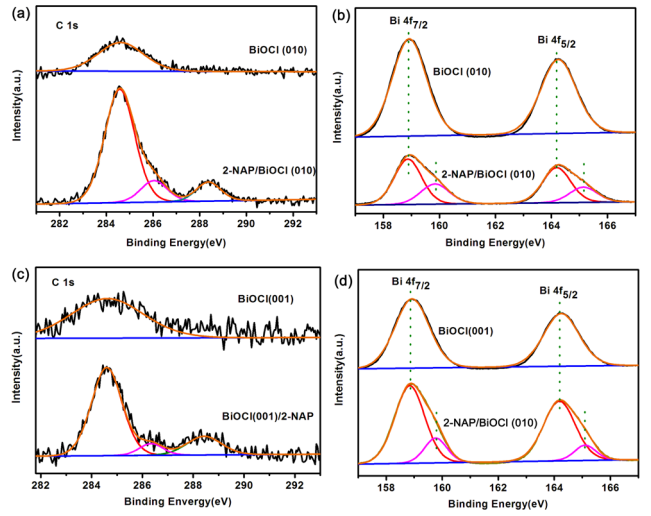

Figure 7. X-ray photoelectron spectroscopy spectra of the samples: (a) (c) C 1s, and (b) (d) Bi 4f.

Obviously, the enriched surface carbon in BiOCl can result from 2-NAP. These data reveal that carbon may substitute for some of the lattice bismuth atoms and form a Bi—O—C structure like Ti—O—C.[38] In regard to 2-NAP/BiOCl (010) and 2-NAP/BiOCl (001), three peaks can be assigned to the C═C/C—C of 2-NAP, the C—H of 2-NAP, and Bi—O—C, which are in good agreement with analogous XPS studies reported previously.[38,39]

The evidence of the Bi—O—C bond formation has been further investigated and proved by analyzing the XPS spectrogram of the Bi (4f) core level, as displayed in Figure 7b,d. Figure 7b shows XPS spectra for bare BiOCl (010) at Bi (4f) binding energy regions. The peaks of binding energies located in 164.2 and 158.9 eV are assigned to the spin orbital splitting photoelectrons of Bi ($4f_{5/2}$) and Bi ($4f_{7/2}$) in the BiOCl, respectively.[40] This splitting energy is 5.3 eV between the Bi ($4f_{5/2}$) and Bi ($4f_{7/2}$), referring to the normal state of BiOCl. The two characteristic bands of 2-NAP/BiOCl (010) at 164.2 and 158.9 eV (relating to the Bi $4f_{5/2}$ and Bi $4f_{7/2}$ peaks) with the same spin energy separation of 5.3 eV and the other two weak bands located in 165.2 eV (Bi $4f_{5/2}$) and 159.8 eV (Bi $4f_{7/2}$) are found in Figure 7b. The Bi (4f) bands slightly shift (0.9 eV) to high binding energies in 2-NAP/BiOCl, which can be attributed to a slight surface charge effect due to polarization variation of the BiOCl nanosheets. And it may be related to the strong chemical bond between BiOCl and 2-NAP. Thus, the binding energy shifts of the Bi signal also verify the perturbation of the Bi-related chemical bonds caused by 2-NAP involvement and probably come out of a Bi—O—C bond, unlike Bi—C, which the Bi(4f) XPS peak shifts to a low binding energy.[32] The peak area shift ratio of BiOCl (010) and BiOCl (001) is 27% and 13%, respectively. The diagnosis data further confirm that abundant terminal bismuth atoms on BiOCl (010) surface are a benefit of the formation of the Bi—O—C bond.

The transient photocurrents are employed to analyze the transformation of photoelectric responses with and without the 2-NAP over the BiOCl nanosheet. Figure 8 shows the transient

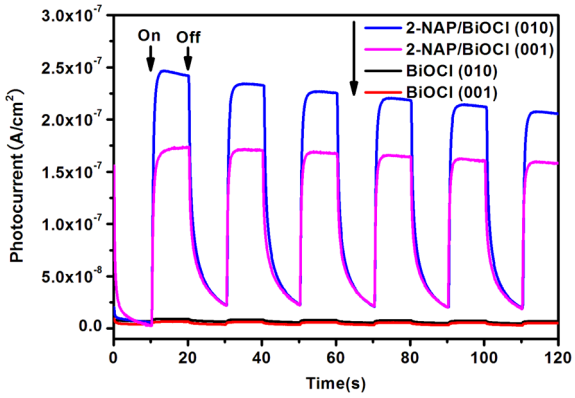

Figure 8. Transient photocurrent responses of the samples in 0.2 M Na_2SO_4 with zero bias versus Ag/AgCl electrodes at illumination by xenon lamp (300 W, $\lambda \geq 420$ nm).

photocurrent responses of the samples carried out to photocatalytic reactions under the intermittent visible light irradiation using the same wavelength region. The result indicates that the photocurrents of the BiOCl/ITO electrodes are negligible under the visible light irradiation. On the other hand, the 2-NAP/BiOCl/ITO electrodes exhibit much larger photocurrents than the BiOCl/ITO electrodes with zero bias versus Ag/AgCl electrodes under visible illumination. It is easy to comprehend that BiOCl cannot be excited by the irradiation of visible light owing to its high band-gap energy. The photocurrents of 2-NAP/BiOCl mostly result from the surface complex, which can be excited via absorbing visible light and subsequently transfer electrons into ITO to generate the photocurrent. Meanwhile, the sequence of the photocurrent strength is in accordance with the order of their photocatalytic performances.

It is known that contributions of active oxygen species, such as superoxide radicals ($O_2^{\bullet -}$) and hydroxyl radicals ($^{\bullet}OH$), are mainly involved in photocatalytic degradation of organic pollutant in water.[1,41] Therefore, in order to explore the essence of active oxygen species formed over 2-NAP/BiOCl(010) system during the visbile light irradiation, the ESR spectra of DMPO−$^{\bullet}OH$ in water-medium and DMPO−$O_2^{\bullet -}$ in methanol-medium have been probed (see Figure 9).[15] The $^{\bullet}OH$ radicals on BiOCl (010) and 2-NAP/BiOCl (010) (see Figure 10) are hardly detected, probably because tiny amounts of $^{\bullet}OH$ radicals or $^{\bullet}OH$ radicals formed quickly reacting with 2-NAP.[42−45] The photocatalytic activity of BiOCl (010) reduces slightly via adding isopropanol (hydroxyl radical scavenger) (Figure S5, Supporting Information).[45] This result is in favor of the hypothesis. And no signals of superoxide radical species are found in BiOCl (010) and BiOCl (001). Interestingly, under visible light irradiation, the intensity signals of the superoxide radical species formed in 2-NAP/BiOCl (010) whereas weaker signals formed in 2-NAP/BiOCl (001). In contrast, no signals are detected without light irradiation.

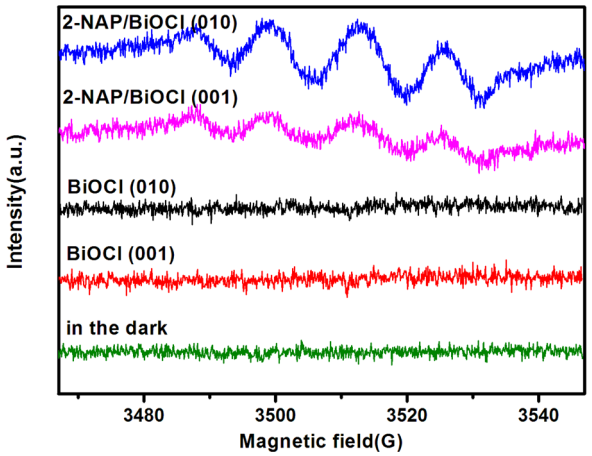

Figure 9. The DMPO−$O_2^{\bullet-}$ adducts are detected for the samples dispersed in methanol.

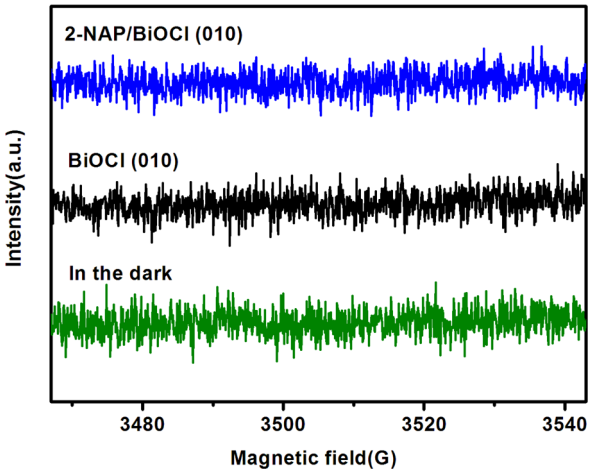

Figure 10. The DMPO−$^{\bullet}$OH adducts are detected for the samples dispersed in water.

The result elucidates that $O_2^{\bullet-}$ is generated on 2-NAP/BiOCl (010) under visbile light irradiation. To further investigate the impact of $O_2^{\bullet-}$ radical species on degradation of 2-NAP over BiOCl (010), the controlled experiments under N_2-saturated conditions have been performed, which can help us to comprehend the potential photocatalytic mechanism. The rate for degradation of 2-NAP over BiOCl (010) remarkably decreases under N_2-saturated conditions as shown in Figure S6 (Supporting Information). The results indicate that, under visible light irradiation, the superoxide radicals and hydroxyl radicals play an important role toward the degradation of 2-NAP over BiOCl (010) nanosheets.

According to all the above experiments, a feasible mechanism for photocatalytic degradation of 2-NAP on a BiOCl nanosheet is proposed, as illustrated in Figure 11. The Bi−O−$C_{10}H_7$ complex is excited under visible light via charge-transfer-complex pathway charge transfer.[42,46] Here electrons are directly transferred from Bi−O−$C_{10}H_7$ to the conduction band of BiOCl. When electrons are injected into the conduction band of BiOCl, they will be transferred to O_2, an electron acceptor, to generate reactive oxygen species (e.g., $O_2^{\bullet-}$, $^{\bullet}$OH), which subsequently cause a series of oxidative degradation reactions of 2-NAP.

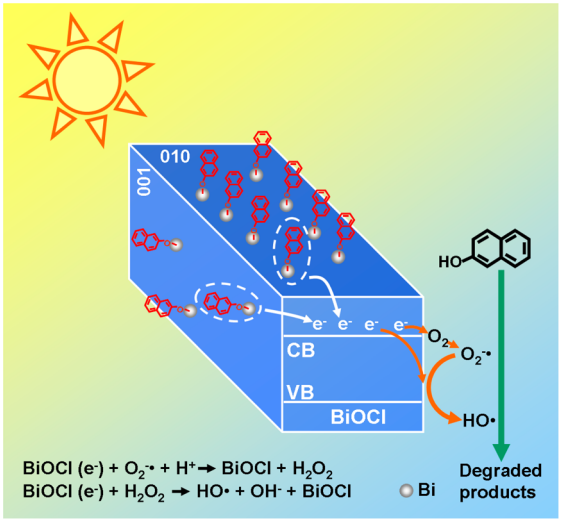

Figure 11. Schematic diagram of the proposed mechanism for degradation of 2-NAP over the BiOCl (010) under visible light irradiation.

4. CONCLUSION

In summary, we report on photoreactivity for photodegradation of colorless dyes on BiOCl nanosheets exposing (010) and (001) facets by an exciton-free and nonsensitized mechanism under visible light. The photocatalytic activities are mainly owing to the formation of surface complex on the BiOCl surface. The result that BiOCl nanosheet exposing (010) facets exhibit higher activity is due to more surface complex formed on the BiOCl (010) surface that consists of more terminal bismuth atoms. Our current work is expected to offer new insight into photocatalytic theory for better understanding photocatalytic reactions and for rational design and synthesis of a photocatalyst with high activity.

■ ASSOCIATED CONTENT

Supporting Information

AQY calculation, reaction rate constants for series of samples, zeta potential and atomic structure of BiOCl with dominant exposed (010) and (001) facets, XRD patterns of BiOCl (010) before and after reaction, the degradation of 2-NAP in the presence of N_2 and isopropahol over BiOCl (010), and the degradation of 1-NAP and 2,3-DN over BiOCl (010) under visible light. This material is available free of charge via the Internet at http://pubs.acs.org.

■ AUTHOR INFORMATION

Corresponding Author

*P. Liu. E-mail: liuping@fzu.edu.cn. Fax: +86 83779239. Tel: +86 83779239.

Notes

The authors declare no competing financial interest.

■ ACKNOWLEDGMENTS

This work is supported by National Natural Science Foundation of China (21173046, 21033003, 21273035, J1103303), National Basic Research Program of China (973 Program: 2013CB632405).

REFERENCES

(1) Hoffmann, M. R.; Martin, S. T.; Choi, W.; Bahnemann, D. W. *Chem. Rev.* **1995**, *95*, 69−96.
(2) Lee, H.; Choi, W. *Environ. Sci. Technol.* **2002**, *36*, 3872−3878.
(3) Long, M.; Cai, W.; Cai, J.; Zhou, B.; Chai, X.; Wu, Y. *J. Phys. Chem. B* **2006**, *110*, 20211−20216.
(4) Tettey, K. E.; Yee, M. Q.; Lee, D. *ACS Appl. Mater. Interfaces* **2010**, *2*, 2646−2652.
(5) Grandcolas, M.; Cottineau, T.; Louvet, A.; Keller, N.; Keller, V. *Appl. Catal., B* **2013**, *138-139*, 128−140.
(6) Sano, T.; Tsutsui, S.; Koike, K.; Hirakawa, T.; Teramoto, Y.; Negishi, N.; Takeuchi, K. *J. Mater. Chem. A* **2013**, *1*, 6489−6496.
(7) Chen, X.; Shen, S.; Guo, L.; Mao, S. S. *Chem. Rev.* **2010**, *110*, 6503−6570.
(8) Osterloh, F. E. *Chem. Mater.* **2008**, *20*, 35−54.
(9) Thornton, J. M.; Raftery, D. *ACS Appl. Mater. Interfaces* **2012**, *4*, 2426−2431.
(10) Maeda, K.; Domen, K. *J. Phys. Chem. Lett.* **2010**, *1*, 2655−2661.
(11) Kubacka, A.; Fernandez-Garcia, M.; Colon, G. *Chem. Rev.* **2012**, *112*, 1555−1614.
(12) Chen, X.; Liu, L.; Yu, P. Y.; Mao, S. S. *Science* **2011**, *331*, 746−750.
(13) Berger, T.; Sterrer, M.; Diwald, O.; Knozinger, E.; Panayotov, D.; Thompson, T. L.; Yates, J. T., Jr. *J. Phys. Chem. B* **2005**, *109*, 6061−6068.
(14) Jiang, J.; Zhao, K.; Xiao, X.; Zhang, L. *J. Am. Chem. Soc.* **2012**, *134*, 4473−4476.
(15) Weng, S.; Chen, B.; Xie, L.; Zheng, Z.; Liu, P. *J. Mater. Chem. A* **2013**, *1*, 3068−3075.
(16) Ye, L.; Zan, L.; Tian, L.; Peng, T.; Zhang, J. *Chem. Commun.* **2011**, *47*, 6951−6953.
(17) Pare, B.; Sarwan, B.; Jonnalagadda, S. B. *Appl. Surf. Sci.* **2011**, *258*, 247−253.
(18) Kim, S.; Choi, W. *J. Phys. Chem. B* **2005**, *109*, 5143−5149.
(19) Zhuang, J.; Dai, W.; Tian, Q.; Li, Z.; Xie, L.; Wang, J.; Liu, P.; Shi, X.; Wang, D. *Langmuir* **2010**, *26*, 9686−9694.
(20) Kamegawa, T.; Seto, H.; Matsuura, S.; Yamashita, H. *ACS Appl. Mater. Interfaces* **2012**, *4*, 6635−6639.
(21) Kamat, P. V. *Chem. Rev.* **1993**, *93*, 267−300.
(22) Wang, R.; Hashimoto, K.; Fujishima, A.; Chikuni, M.; Kojima, E.; Kitamura, A.; Shimohigoshi, M.; Watanabe, T. *Nature* **1997**, *388*, 431−432.
(23) Henderson, M. A.; White, J. M.; Uetsuka, H.; Onishi, H. *J. Am. Chem. Soc.* **2003**, *125*, 14974−14975.
(24) Lu, G.; Linsebigler, A.; Yates, J. T. *J. Phys. Chem.* **1994**, *98*, 11733−11738.
(25) Ohtani, B. *Chem. Lett.* **2008**, *37*, 216−229.
(26) Yang, H. G.; Sun, C. H.; Qiao, S. Z.; Zou, J.; Liu, G.; Smith, S. C.; Cheng, H. M.; Lu, G. Q. *Nature* **2008**, *453*, 638−641.
(27) Liu, G.; Yu, J. C.; Lu, G. Q.; Cheng, H. M. *Chem. Commun.* **2011**, *47*, 6763−6783.
(28) Henderson, M. A.; Lyubinetsky, I. *Chem. Rev.* **2013**, *113*, 4428−4455.
(29) Zuo, F.; Bozhilov, K.; Dillon, R. J.; Wang, L.; Smith, P.; Zhao, X.; Bardeen, C.; Feng, P. *Angew. Chem., Int. Ed.* **2012**, *51*, 6223−6226.
(30) D'Arienzo, M.; Carbajo, J.; Bahamonde, A.; Crippa, M.; Polizzi, S.; Scotti, R.; Wahba, L.; Morazzoni, F. *J. Am. Chem. Soc.* **2011**, *133*, 17652−17661.
(31) Zang, S.; Lian, B. *J. Hazard. Mater.* **2009**, *166*, 33−38.
(32) Gao, F.; Zeng, D.; Huang, Q.; Tian, S.; Xie, C. *Phys. Chem. Chem. Phys.* **2012**, *14*, 10572−10578.
(33) Szostak, M. M.; Natkaniec, I. *J. Raman Spectrosc.* **1989**, *20*, 493−501.
(34) Zhang, K.; Liang, J.; Wang, S.; Liu, J.; Ren, K.; Zheng, X.; Luo, H.; Peng, Y.; Zou, X.; Bo, X.; Li, J.; Yu, X. *Cryst. Growth. Des.* **2012**, *12*, 793−803.
(35) Geng, J.; Hou, W. H.; Lv, Y. N.; Zhu, J. J.; Chen, H. Y. *Inorg. Chem.* **2005**, *44*, 8503−8509.
(36) Shamaila, S.; Sajjad, A. K.; Chen, F.; Zhang, J. *J. Colloid Interf. Sci.* **2011**, *356*, 465−472.
(37) Tian, Y.; Guo, C. F.; Guo, Y.; Wang, Q.; Liu, Q. *Appl. Surf. Sci.* **2012**, *258*, 1949−1954.
(38) Ren, W.; Ai, Z.; Jia, F.; Zhang, L.; Fan, X.; Zou, Z. *Appl. Catal., B* **2007**, *69*, 138−144.
(39) Li, Z.; Shen, Y.; Yang, C.; Lei, Y.; Guan, Y.; Lin, Y.; Liu, D.; Nan, C.-W. *J. Mater. Chem. A* **2013**, *1*, 823−829.
(40) Song, J.-M.; Mao, C.-J.; Niu, H.-L.; Shen, Y.-H.; Zhang, S.-Y. *CrystEngComm* **2010**, *12*, 3875−3881.
(41) Hirakawa, T.; Nosaka, Y. *Langmuir* **2002**, *18*, 3247−3254.
(42) Wang, N.; Zhu, L.; Huang, Y.; She, Y.; Yu, Y.; Tang, H. *J. Catal.* **2009**, *266*, 199−206.
(43) Litter, M. *Appl. Catal., B* **1999**, *23*, 89−114.
(44) Zhao, J.; Wu, T.; Wu, K.; Oikawa, K.; Hidaka, H.; Serpone, N. *Environ. Sci. Technol.* **1998**, *32*, 2394−2400.
(45) Li, W.; Li, D.; Lin, Y.; Wang, P.; Chen, W.; Fu, X.; Shao, Y. *J. Phys. Chem. C* **2012**, *116*, 3552−3560.
(46) Agrios, A. G.; Gray, K. A.; Weitz, E. *Langmuir* **2004**, *20*, 5911−5917.